Mechanism of the α-ϵ phase transformation in iron

A. Dewaele,[1] C. Denoual,[1] S. Anzellini,[1] F. Occelli,[1] M. Mezouar,[2] P. Cordier,[3] S. Merkel,[3] M. Véron,[4] and E. Rausch[4]

[1]*Commissariat à l'Energie Atomique, Direction des Applications Militaires, Ile de France, F-91297 Arpajon, France*

[2]*European Synchrotron Radiation Facility, BP220, 38043 Grenoble Cedex, France*

[3]*Unité Matériaux et Transformations, Université Lille 1, UMR CNRS 8207, F-59655 Villeneuve d'Ascq Cedex, France*

[4]*Laboratoire SIMaP, Grenoble INP-CNRS-UJF, BP 75, 38402 Saint Martin d'Hères Cedex, France*

(Received 23 June 2014; revised manuscript received 10 March 2015; published 14 May 2015)

The α-Fe $\leftrightarrow$ ϵ-Fe pressure-induced transformation under pure hydrostatic static compression has been characterized with *in situ* x-ray diffraction using α-Fe single crystals as starting samples. The forward transition starts at 14.9 GPa, and the reverse at 12 GPa, with a width of α-ϵ coexistence domain of the order of 2 GPa. The elastic stress in the sample increases in this domain, and partially relaxes after completion of the transformation. Orientation relations between parent α-Fe and child ϵ-Fe have been determined, which definitely validates the Burgers path for the direct transition. On the reverse transition, an unexpected variant selection is observed. X-ray diffraction data, complemented with *ex situ* microstructural observations, suggest that this selection is caused by defects and stresses accumulated during the direct transition.

DOI: 10.1103/PhysRevB.91.174105 PACS number(s): 61.50.Ks, 07.35.+k, 81.30.Kf

I. INTRODUCTION

The pressure-induced α-Fe (body-centered-cubic, bcc) $\rightarrow$ ϵ-Fe (hexagonal close-packed, hcp) phase transformation, observed around 13 GPa at 295 K, is considered as an archetypal martensitic transition (a diffusionless military structural transformation in a solid). It has profound implications in Fe-based materials technology, fundamental condensed-matter science—in particular, its relation with magnetism, and Earth's sciences—with iron being the main component of terrestrial planetary cores. Early experiments have established its first-order and athermal character [1–3]. A bcc-hcp transformation is, by nature, *reconstructive* (the child symmetry group is not a subgroup of the parent symmetry group), and it is expected that the initial microstructure is not recovered after a transformation cycle—which is called "irreversibility" [4,5]. Recently, information on the α-Fe $\leftrightarrow$ ϵ-Fe mechanism have been collected using static [6–9] and dynamic [10–12] compression. Several pieces of evidence [7–10,12] point to a mechanism initially proposed by Burgers for the α-Zr $\leftrightarrow$ β-Zr transformation [13], hereafter called Burgers path. However, these pieces of evidence are indirect or partial. The driving forces for the transformation are not clearly understood. If *ab initio* calculations predict that the enthalpy of ϵ-Fe becomes lower than the enthalpy of α-Fe around 10 GPa [14–16], the calculated energy barrier along Burgers path is too high to allow the system to undergo the phase transformation below $\simeq$30 GPa [14,16], which is significantly higher than experimentally observed. Magnetic interactions or a heterogeneous transformation could reduce this barrier [17–19]. On the experimental side, the sensitivity of the onset of direct and reverse transformations to nonhydrostatic stress [20] has raised the question regarding its influence on the transformation mechanism [14], also suggesting that additional attention has to be paid for the experimental procedure to guide the models.

Here we report experimental observation made on a system designed to avoid the possible effects of a complex initial microstructure (such as dislocation saturated polycrystal) and nonhydrostatic loading, thus reducing the gap between experiments and first-principles calculations. High-purity single crystals of α-Fe have been compressed hydrostatically in diamond-anvil cells and characterized *in situ* with x-ray diffraction (XRD) during multiple α-Fe $\leftrightarrow$ ϵ-Fe cycles. Orientation relations between the parent and child phases have been determined and are discussed in the context of the Burgers path. Microstructural observations have been carried out on recovered samples to help understand the XRD observations.

II. METHODS

Single-crystal discs of iron of less than 20 μm thickness and 30 to 40 μm diameter, with the surface normal parallel to the [001] direction, were cut [21] from a bulk single crystal (99.98% purity, Mateck) and heat treated (700 K during 8 hours under vacuum). Three samples were loaded in a helium or neon pressure medium, with ruby or SrB_4O_7 : Sm^{2+} pressure gauges, in diamond-anvil cells. The historical pressure calibration [22,23] of these gauges has been used for the homogeneity of data with earlier studies [6,20]. In the scanned pressure range, the difference of pressure between Ref. [22] and more recent calibrations [24] remains smaller than 0.2 GPa. The uncertainty of the pressure estimate using these gauges is smaller than 0.3 GPa in the studied range, which includes uncertainty of the luminescence wavelength measurement and of the pressure calibration [24]. We checked with interferometry [25] that the gap between the anvils was at least $\simeq$5 μm higher than the sample thickness, so that the sample was embedded in the pressure medium. This was also checked in the course of the experiment. For each sample, the pressure has been cycled between $\simeq$5 and $\simeq$19 GPa a few times, at 300 or 380 K.

At each pressure step, after pressure stabilization, angular-dispersive XRD (wavelength 0.3738 Å, 2×3 μm spot) patterns were recorded while rotating the diamond-anvil cell by at least 30° around a vertical axis (angle θ_C) by steps of 0.2° to 1° [see Fig. 1(a)]. One composite image obtained by summing the individual diffraction images of the sample is shown in Fig. 1(b). The α-Fe samples are flawless bcc single crystals with no noticeable distortions, as demonstrated by the small diffraction peak width [see Fig. 1(b)]. As expected

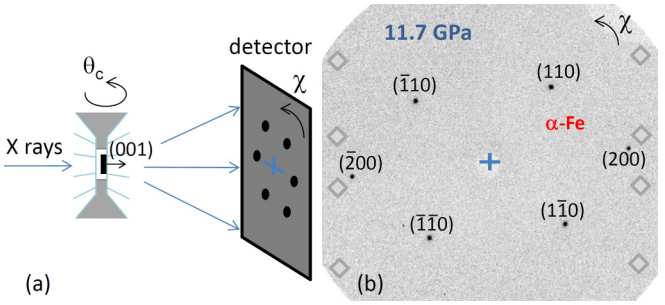

FIG. 1. (Color online) (a) Sketch of the x-ray diffraction (XRD) setup. The monochromatic x-ray beam is focused on the sample (in black) which can be rotated by θ_C around a vertical axis. The diffracted signal is recorded on a bidimensional detector. The incoming x-ray beam position (cross) and azimuthal angle χ are indicated. (b) Composite x-ray diffraction image of the sample after pressure increase to 11.7 GPa. The (hkl) Miller indices of the Bragg spots of α-Fe are indicated. Gray diamonds hide the XRD signal of the diamond anvils.

from the orientation of the bulk starting single crystal, the diamond-anvil surfaces are perpendicular to a (001) direction of α-Fe.

In order to ensure purely hydrostatic compression of the sample, pressures cycles at 380 K were performed in a liquid helium pressure medium for one run [26]. The two other runs have been performed at 300 K, in a helium or neon pressure medium. At this temperature, neon and helium are solid above 5.5 and 12.0 GPa, respectively [26]. Evidence that nonhydrostatic stresses develop in a neon and helium pressure media has been collected above 15 and 25 GPa, respectively [27,28], at 300 K. We therefore call the runs performed at 300 K "quasihydrostatic" because small amounts of nonhydrostatic stress may have developed in the pressure medium for these runs. The purely hydrostatic and quasihydrostatic runs lead to similar observations, as detailed below.

III. CONDITIONS OF THE TRANSFORMATION

All diffraction peaks of the same class were observed at the same diffraction angle 2θ in α-Fe and ϵ-Fe. Consequently, bidimensional XRD spectra were azimuthally integrated and treated as polycrystal patterns to determine phase fractions and measure the lattice parameters of both phases. Figure 2 presents integrated patterns for the pure hydrostatic loading run; α-Fe and ϵ-Fe can be easily identified and their fraction has been estimated using the intensity ratio between $(002)_{bcc}$ and $(10\bar{1}2)_{hcp}$ peaks. The evolution of the full width at half maximum (FWHM) of the $(110)_{bcc} + (0002)_{hcp}$ peaks with pressure is presented in Fig. 3. Figure 4 presents the evolution of the ϵ-Fe fraction for the three experimental runs.

The onset of the direct $\alpha \rightarrow \epsilon$ transition is sensitive to the pressurizing conditions: it begins at 14.9 GPa in pure hydrostatic compression (helium at 380 K) starting in a single crystal, which can be considered as a reference value. In solid helium at 300 K, the transition starts around 14.2 GPa. For the less hydrostatic pressurizing conditions (neon at 300 K), the direct transition starts at 13.8 GPa. The reverse $\epsilon \rightarrow \alpha$

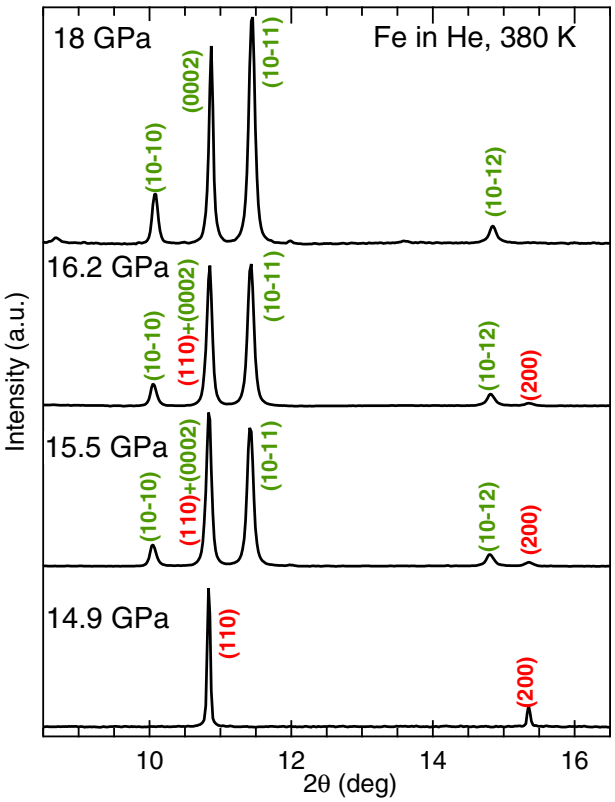

FIG. 2. (Color online) 1D patterns obtained by azimuthal integration of the XRD images recorded using a liquid helium pressure transmitting medium at 380 K. The Miller indices of the XRD lines for α-Fe and ϵ-Fe are indicated in red and green, respectively.

transition, or reversion, begins at 12 GPa in hydrostatic conditions. This large hysteresis is characteristic of the martensitic mechanism which involves a large elastic energy associated with the transformation strain. Minor amounts of α-Fe (ϵ-Fe) remain above 18 GPa (under 8.7 GPa). The average midpoint between the forward and reverse transformation is 13.1 GPa, which is consistent with earlier static data obtained under varying pressurizing conditions [6,20].

The ϵ-α coexistence domain is very narrow for the first direct transition, which starts in a α-Fe single crystal: $\simeq$80%

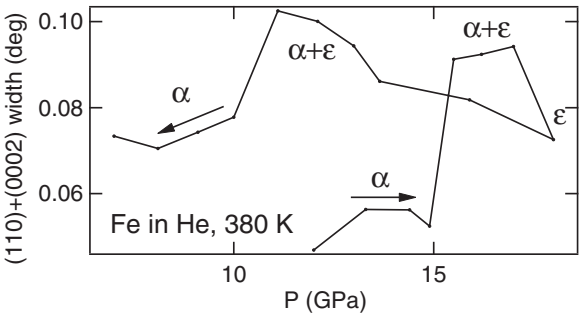

FIG. 3. Two-θ full width at half maximum of $(110)_{bcc} + (0002)_{hcp}$ XRD peaks during the first pressure cycle for the hydrostatic run (see Fig. 2). The arrows indicate in which order the data have been taken. The Greek letters indicate at which conditions α-Fe and ϵ-Fe are observed.

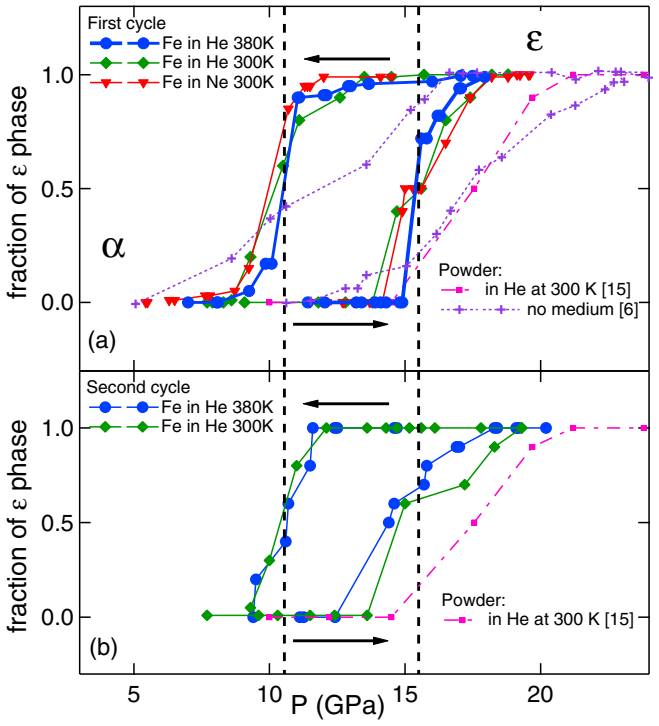

FIG. 4. (Color online) Fraction of ϵ-Fe on pressure increase and decrease for three runs, for (a) the first and (b) the second pressure cycle. It has been estimated using the intensity ratio between $(002)_{bcc}$ and $(10\bar{1}2)_{hcp}$ peaks. Different symbols and colors correspond to different runs. The symbol size corresponds to the uncertainty in pressure. The vertical dashed lines indicate the pressure for direct and reverse transitions. Literature data obtained using powder samples are also plotted as purple dotted lines (nonhydrostatic loading, Ref. [6]) and dash-dotted pink line and symbols (hydrostatic loading, Ref. [15]).

of the sample is transformed in a 0.6 GPa pressure step under hydrostatic conditions [see Figs. 2 and 4(a)]. The second direct transition (which starts in the reversed α-Fe phase) is more sluggish, as evidenced in Fig. 4(b): the coexistence domain has the same width (although slightly shifted) as for a powder sample compressed in quasihydrostatic conditions (Ref. [15], dash-dotted line in Fig. 4). It remains much narrower than under nonhydrostatic compression [Ref. [6], dotted lines in Fig. 4(a)]. The coexistence domains for the reversion are similar for the first and second pressure cycles.

IV. ELASTIC STRESSES IN α-Fe AND ϵ-Fe

The measurements performed in a neon pressure medium at 300 K are plotted in Fig. 5 together with literature measurements [6,15], and listed in Table I. The measurements of the two other runs are not plotted for the clarity of the graph, but yielded similar results. The $P-V$ and c/a data obtained for pure α-Fe and ϵ-Fe samples agree with a previous study [15]. In the following discussion, we will focus on the measurements made in the domain of coexistence of ϵ-Fe and α-Fe.

The early work of Ref. [6], performed on a nonhydrostatically compressed powder sample, reports an anomalously high value of the c/a ratio in this domain (see Fig. 5, green

TABLE I. Atomic volume V measured in bcc α-Fe ($V = a^3/2$) and hcp ϵ-Fe ($V = a^2c\sqrt{3}/4$) and c/a ratio measured in ϵ-Fe during one run (in a neon pressure medium at 300 K), during the first pressure cycle. In the domain of coexistence of α-Fe and ϵ-Fe, the volumes have been calculated using $(002)_{bcc}$, $(10\bar{1}0)_{hcp}$, and $(10\bar{1}2)_{hcp}$ XRD peaks. The data are presented in the order they have been taken.

P (GPa)	V_{bcc} (Å^3/at)	V_{hcp} (Å^3/at)	c/a_{hcp}	P (GPa)	V_{bcc} (Å^3/at)	V_{hcp} (Å^3/at)	c/a_{hcp}
Pressure increase				Pressure decrease			
12.7	11.052			14.5		10.393	1.6060
13.1	11.025			11.6		10.517	1.6067
13.1	11.022			11.4		10.527	1.6067
13.6	11.003			11.3		10.531	1.6068
13.9	10.992			10.8	11.190	10.569	1.6069
14.3	10.980			9.4	11.190	10.672	1.6097
14.7		10.387	1.6091	8.7	11.213	10.699	1.6143
15.0	10.946	10.384	1.6090	7.6	11.269		
15.3	10.927	10.373	1.6083	6.5	11.330		
15.8	10.924	10.354	1.6080	5.4	11.409		
16.7	10.905	10.321	1.6064	6.1	11.379		
17.5	10.901	10.295	1.6061				
18.3		10.27	1.6054				
19.0		10.246	1.6048				
19.4		10.226	1.6047				

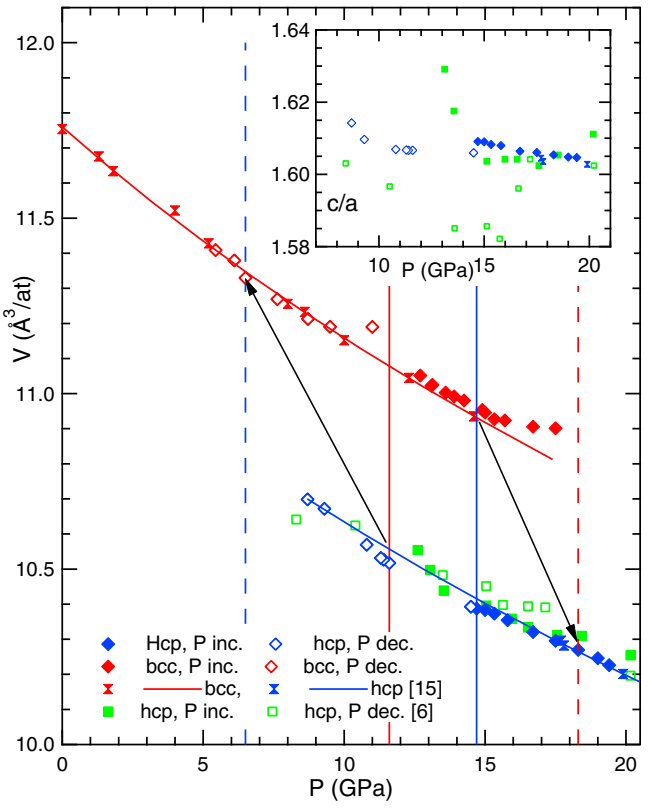

FIG. 5. (Color online) Volume of α-Fe and ϵ-Fe measured on pressure increase (inc.) and decrease (dec.), in one run (in a neon pressure medium, $T = 300$ K). The vertical continuous (dashed) lines indicate the pressure of appearance (disappearance) of ϵ-Fe (in blue) and α-Fe (in red). Inset: evolution of the c/a ratio in ϵ-Fe. The corresponding data are listed in Table I. Data from Refs. [6] and [15] are also plotted as points and dash-dotted lines.

symbols). A similar effect is reported in Ref. [29]. Such a behavior witnesses large elastic distortions in the ϵ-Fe lattice, which had been interpreted with a $(100)_{bcc} \parallel (1\bar{2}10)_{hcp}$ epitaxial growth [6] or with an intermediate face-centered-cubic structure [29]. This is not observed here: the c/a ratio in ϵ-Fe exhibits smooth variations on pressure increase, which is consistent with the trend measured in the stability field of ϵ-Fe [15]. On pressure decrease, a slight increase of c/a is observed when the amount of ϵ-Fe in the sample becomes smaller than 20%. The fact that it appears only on pressure decrease suggests that this distortion is not directly linked to the transformation mechanism as suggested in Ref. [6], but to an accumulation of elastic stresses in the minority phase. An increase of c/a by 0.008, as measured, corresponds roughly to an elastic uniaxial stress of 1.5 GPa [30], which is of the same order of magnitude as the yield stress of polycrystalline ϵ-Fe [31].

The volume of ϵ-Fe plotted in Fig. 5 does not show any anomalies. α-Fe volume becomes slightly greater than the extrapolated one for pure α-Fe [15] (dashed line) when the fraction of α-Fe decreases, with the extra elastic energy being likely balanced by the enthalpy gain of $\alpha - \epsilon$ transformation. This emphasizes the nonequilibrium nature of this transition during the coexistence of the α and ϵ phases. We stress that the volume of α-Fe is evaluated from only one diffraction line: $(002)_{bcc}$, i.e., compression along (002) and hydrostatic compression cannot be discriminated.

The width in diffraction angle 2θ of $(110)_{bcc} + (0002)_{hcp}$ XRD peaks increases in the domain of coexistence (Fig. 3), which is another evidence of an elastic stress in both phases (see Sec. VII). After reversion, the 2θ width of $(110)_{bcc}$ peaks is only slightly higher than in the initial crystal ($\sim$0.07° FWHM; see Fig. 3).

V. MICROSTRUCTURE OF ϵ-Fe

The Burgers path for a bcc $\rightarrow$ hcp transformation can be described by a lattice distortion and a shuffle, in addition to pure hydrostatic compression [see Fig. 6(a)]. The lattice distortion is a combination of a compression in the $(110)_{bcc}$ plane along the $[001]_{bcc}$ direction so that atoms form regular hexagons that will become $(0001)_{hcp}$ planes. Then every other $(110)_{bcc}$ plane shuffles by $a_{bcc}/(3\sqrt{2})$ in the $[\bar{1}10]_{bcc}$ direction to form a hcp structure. An additional sketch along $[110]_{bcc}$ modifies the c/a up to the value needed for the hcp lattice. In a bcc lattice, there are six equivalent (110) planes, and therefore six different hcp crystals (called *variants*) can be obtained with this mechanism. This transformation, when applied to numerous grains of different orientations, may induce strong deviatoric stress that must be relaxed through a plastic activity. The system limits the atomic displacements by leaving unchanged the plane $(1\bar{1}2)_{bcc} \parallel (10\bar{1}0)_{hcp}$ during the compression. This results in a rotation of the $(1\bar{1}00)_{hcp}$ and $(01\bar{1}0)_{hcp}$ planes of $\simeq 5°$ around the $\vec{c}$ axis (and of $-5°$ if the orientation of $(01\bar{1}0)_{hcp}$ is kept). This additional rotation splits each variant into two crystal orientations differing by a rotation of 10° around the $\vec{c}$ axis, leading to a total of 12 crystal orientations. Table II lists some orientation relations between the initial bcc and final hcp lattice planes when the path represented in Fig. 6(a) is followed.

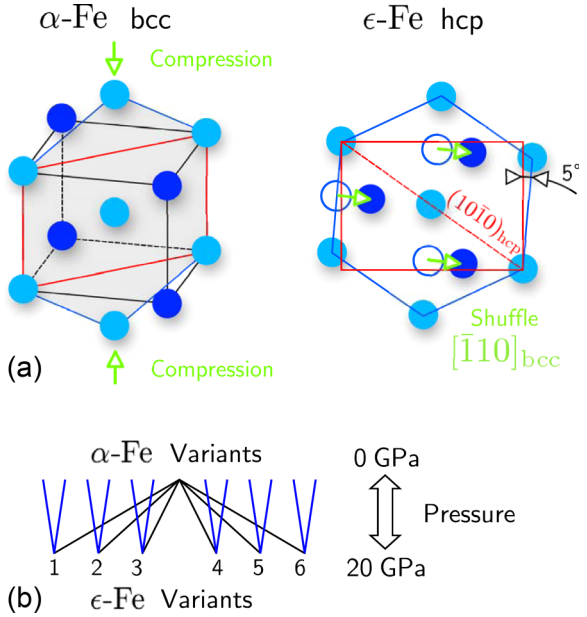

FIG. 6. (Color online) (a) Burgers path for the α-Fe $\rightarrow$ ϵ-Fe transformation (see text). The gray plane on the left is the $(110)_{bcc}$ plane, which will transform to the $(0001)_{hcp}$ plane. The green arrows on the left indicate the direction of $[001]_{bcc}$ compression; on the right, they represent the translation vector for the shuffle (translation of the entire plane containing dark blue atoms). (b) Expected evolution of the number of variants during one $\alpha \rightarrow \epsilon \rightarrow \alpha$ cycle. One α-Fe variant transforms into 6 ϵ-Fe variants and then 13 α-Fe variants.

Figure 7 represents the evolution of the composite XRD images recorded in one quasihydrostatic run, during two pressure cycles. ϵ-Fe child variants exhibit a texture clearly inherited from the orientation of the starting single crystal. For instance, in the XRD image in Fig. 7(b), the azimuthal angle χ of all peaks of class $(10\bar{1}0)_{hcp}$ and most peaks of class $(10\bar{1}1)_{hcp}$ are close to the azimuthal angle of the peaks of class $(110)_{bcc}$. The XRD peaks of the ϵ-Fe phase have a FWHM of several degrees in χ, to be compared to 0.18° for the initial α-Fe sample. The "rocking curve," i.e., the intensity of the XRD peak vs θ_C, is also dramatically enlarged by the α-Fe to ϵ-Fe transformation, evidencing a large plastic strain [Fig. 8(b)]. The XRD peaks of the remaining α-Fe also drastically broaden [Fig. 7(b)] when ϵ-Fe appears, suggesting that the transformed zones also induce a large plastic deformation of the remaining untransformed α-Fe.

TABLE II. Some bcc α-Fe planes and the corresponding hcp ϵ-Fe after the transformation which follows the Burgers path represented in Fig. 6(a). For this variant, $(0001)_{hcp}$ is parallel to $(110)_{bcc}$. The five other variants correspond to $(0001)_{hcp}$ parallel to $(1\bar{1}0)_{bcc}$, $(011)_{bcc}$, $(01\bar{1})_{bcc}$, $(101)_{bcc}$, and $(10\bar{1})_{bcc}$.

bcc phase	hcp phase	Disorientation
(110)	(0001)	none
$(1\bar{1}0)$	$(1\bar{1}00)$	5°
$(1\bar{1}2)$	$(10\bar{1}0)$	none
(101)	$(\bar{1}011)$	none

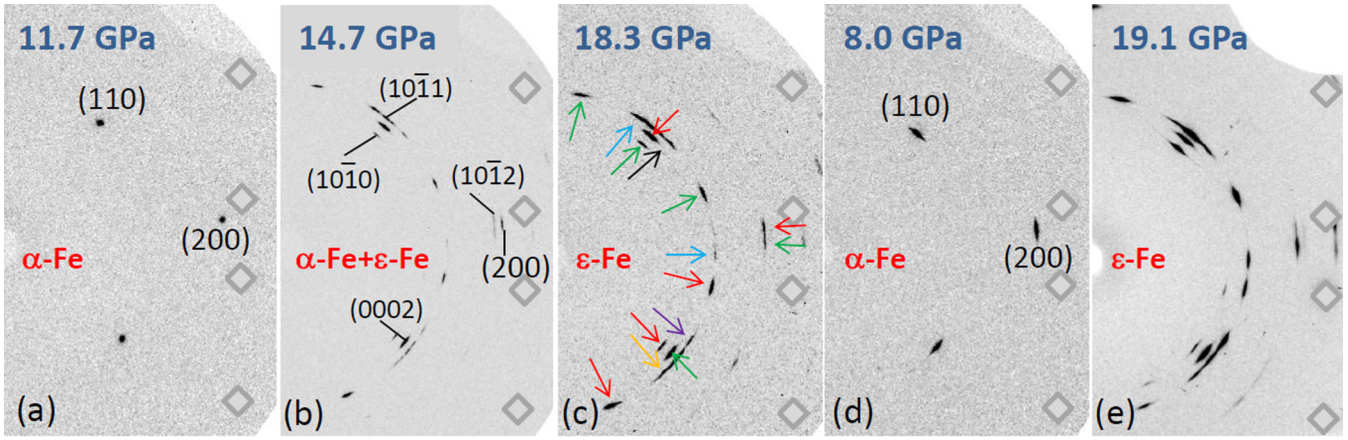

FIG. 7. (Color online) Details of composite XRD images (see Fig. 1 for the setup) presented in the order they have been taken during two pressure cycles in one run (in a helium pressure medium, at 300 K). The gray diamonds hide the XRD signal of the diamond anvils. The observed Fe phase(s) are indicated in red. Miller indices of α-Fe (hkl) and ϵ-Fe $[hk(-h-k)l]$ are specified in (a), (b), and (d). In (c), arrows of six different colors point to the main ϵ-Fe XRD spots: each color identifies two close orientations of a pseudosingle crystal (see text).

Focusing on the main orientation of each XRD peak recorded in one composite image, we have determined whether different peaks belonged to the same (although distorted by the dislocation network) single crystal of ϵ-Fe. For that purpose, the orientation of each peak was determined in the referential of the sample, using data such as those plotted in Fig. 8.

We have identified 12 different ϵ-Fe crystal orientations, appearing in six peak sets, split by approximately 10° (see Fig. 8). The XRD peaks of each set are identified with arrows of one color in Fig. 7(c). On the basis of these observations, we can describe the ϵ-Fe sample under pressure as a mixture of single crystals with a limited number (12) of different orientations, which contain a high defect density that enlarges their XRD peaks, hereafter called "pseudosingle crystals."

We have checked that these 12 orientations correspond to the ones predicted by the Burgers path. This definitely validates this path for the α-Fe $\rightarrow$ ϵ-Fe transformation under pure hydrostatic compression. The same conclusion was drawn on the basis of *ex situ* microstructural observation of a polycrystal of α-Fe recovered after uniaxial shock loading above 15 GPa [12]. Our observation provides a direct *in situ* evidence for this mechanism.

In the case of a uniaxial dynamic loading of a single crystal along the $[001]_{bcc}$ direction, the two variants which correspond to $(110)_{bcc} \parallel (0001)_{hcp}$ and $(1\bar{1}0)_{bcc} \parallel (0001)_{hcp}$ have been observed, which evidences a selection of the variants with the compression (first step in Fig. 6) direction parallel to the loading axis [10,32]. In the current experiments, the situation is very different as the transition proceeds under hydrostatic loading. No compression direction is then favored and all variants are observed. The Burgers path involves two steps but it is possible that the system follows a more complex path which couples compression and shear, as modeled in Ref. [16], which allows the transformation with a lower strain than represented in Fig. 6. In one recent study, the static compression of an iron single crystal compressed in a daphne oil pressure medium in a diamond-anvil cell results in the formation of only four variants of ϵ-Fe [9]. This is probably related to a complex nonhydrostatic stress in these experiments.

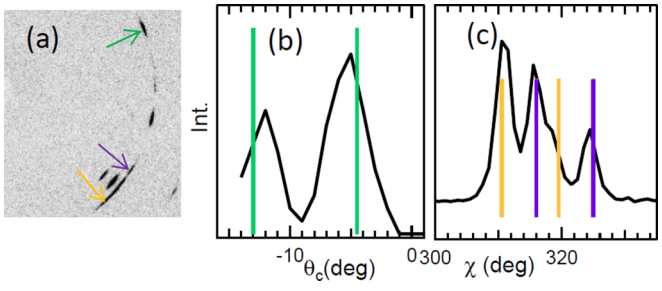

FIG. 8. (Color online) (a) Detail of the composite XRD image from Fig. 7(c). (b) Rocking curve of the $(10\bar{1}1)_{hcp}$ peak indicated with a green arrow. The vertical bars correspond to the peak positions for two close ϵ-Fe orientations predicted by the Burgers path. (c) Profile in χ azimuthal angle of the $(10\bar{1}1)_{hcp}$ peaks indicated with yellow and purple arrows. The vertical bars correspond to the peaks positions for four ϵ-Fe orientations predicted by the Burgers path.

VI. MICROSTRUCTURE OF α-Fe AFTER THE REVERSE TRANSITION

The observations made on reversion are much more surprising. Only one α-Fe pseudosingle crystal with an orientation identical to the initial single crystal is formed on pressure decrease [see Fig. 7(d)]. Very weak XRD peaks corresponding to another variant of α-Fe could be observed in some places of the sample. Further cycles lead to similar observations.

The recovering of one pseudosingle crystal of α-Fe with the same orientation as the starting sample after one α-ϵ-α cycle reminds one of the behavior of shape-memory alloys, for which all variants can only revert in the initial parent phase, leading to an almost complete recovery of the sample initial shape. This behavior is unexpected for a reconstructive martensitic transformation such as the α-Fe $\leftrightarrow$ ϵ-Fe transition [4]. The symmetries of hcp crystal allow for up to three bcc variants to be produced, one with the same orientation as the original α crystal, and two with $(112)_{bcc}$ twinned relationships [12]. Cycling between phases should produce an increasing set

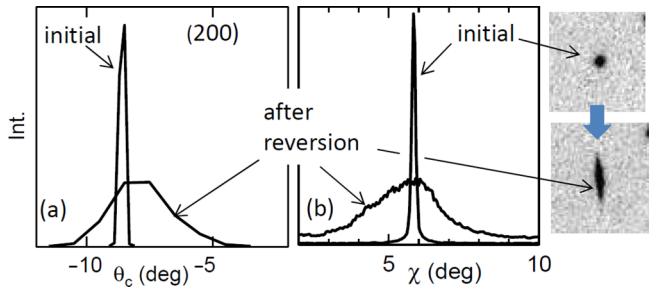

FIG. 9. (Color online) (a) Rocking curves of the $(200)_{bcc}$ XRD peaks represented in Fig. 7(a), starting sample, and Fig. 7(d), after reversion. (b) Profile in χ azimuthal angle of the same peaks.

of reversion α variants [Fig. 6(b)] and an unambiguous irreversible behavior. Indeed, no variant selection at the reversion has been reported in shock compression studies [11,12]: numerous $(112)_{bcc}$ twins are observed in recovered α-Fe. Our observations indicate that the $\alpha \leftrightarrow \epsilon$ transformation under hydrostatic conditions in a Fe single crystal is mostly reversible. Texture or single-crystal memory effects have been reported for the temperature-induced α (hcp) $\leftrightarrow \beta$ (bcc) transition in titanium [33], which may be related to the elastic soft modes observed at the onset of the transition. This is not the case in iron.

The XRD setup used in these experiments is not designed to accurately measure the dislocation density in the sample. However, the rocking curves measured in α-Fe (see Fig. 9) allow for a semiquantitative analysis [34]. The initial α-Fe sample has a rocking curve FWHM of 0.2°, similar to the FWHM for the diamond anvils which are nearly perfect single crystals. The rocking curve of α-Fe pseudosingle crystal after the reversion has a width of 3.5°. Neglecting the instrumental broadening, a multiplication of the dislocation density by a factor of 300 can be inferred [34]. The real multiplication factor for dislocation density is probably much higher, with the initial width being probably mostly due to instrumental broadening.

In order to understand the variant selection at the reversion, we have studied the microstructure of recovered samples. Two samples (runs in helium) have been kept after the experiment to be characterized with transmission electron microscopy (TEM). For these samples, two pressure cycles had been imposed. Thin sections of 40×8 μm were extracted from the samples using a scanning electronic microscope equipped with focused ion beam column. They have been observed by TEM using conventional imaging and the orientation mapping (using ASTAR by NanoMEGAS) technique [35]. The TEM bright field and orientation map in Fig. 10 show that one orientation of α-Fe largely dominates, and a high density of dislocations is observed in this pseudosingle crystal, confirming *in situ* XRD observations. The defects density was too high to be measured using conventional TEM techniques. A few lenticular inclusions are disoriented from the matrix pseudosingle crystal. Since their shape is similar to the transformed zones in dynamic experiments [11,12], we propose that each of these inclusions has been produced by the reversion of one pseudosingle crystal of ϵ-Fe with the same shape. Indeed, different variants of ϵ produce distinct variants

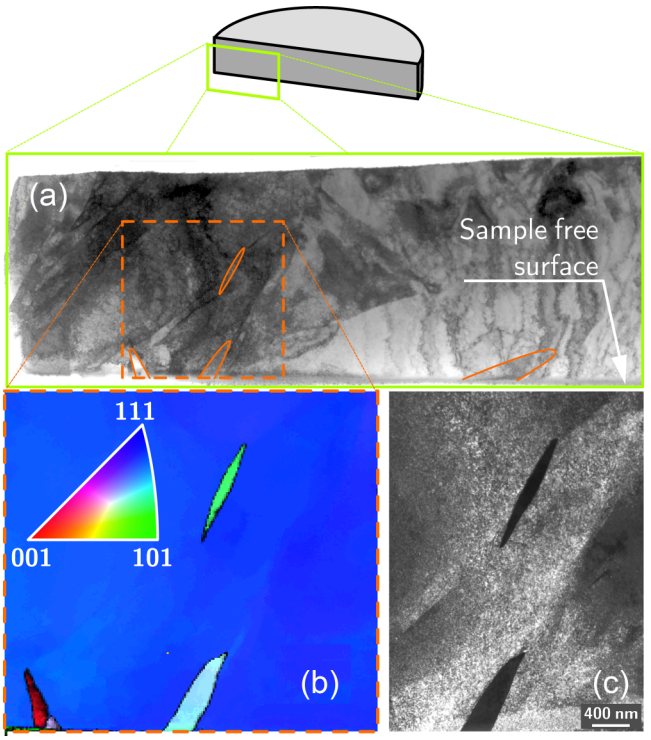

FIG. 10. (Color online) Sample recovered after two transformation cycles, in helium at 300 K. (a) TEM bright field. The sample contains a large density of dislocations which makes the observation of the microstructure very difficult. Variants of α with modified orientation are bordered in red. (b) Orientation map obtained in the TEM-ASTAR. The color in the inverse pole figure map corresponds to the crystallographic orientation of the horizontal direction in the observed plane. Color variations in the background correspond to slight misorientations due to the presence of dislocations. (c) TEM dark field of the same zone. In this mode, dark lenses correspond to variants with a different orientation.

of α—apart from the initial phase (Fig. 6), the reverted α must come from one single lenticular ϵ. In opposition to the observations in Ref. [12], twins or internal structures are rare inside these inclusions. Defects inside the α-Fe matrix can also be seen [Figs. 10(a) and 10(c)], likely inherited from the ϵ-Fe microstructure.

VII. DISCUSSION

The following scenario can be proposed on the basis of *in situ* and *ex situ* observations. On pressure increase, lenticular crystals of ϵ-Fe (typical length 1–10 μm, width 0.2–1 μm, similar to Ref. [12]) nucleated heterogeneously within the single crystal α-Fe matrix at 14.9 GPa, creating a large plastic strain in the whole sample volume evidenced by rocking curves broadening and TEM observation of recovered samples (large density of dislocations). Plastic strain is usual for transformations with a large volume change and where no softening of elastic constants happens in the parent phase, as in iron [14]. The current measurements demonstrate that nonhydrostatic stress is not necessary to drive the transition around 15 GPa, contradicting earlier theoretical proposals [14]. The transition completed on pressure increase, creating a

microstructure of lenticular ϵ-Fe grains. These grains have the 12 crystalline orientations predicted by the Burgers path.

Elastic stress in the sample increased in the domain of coexistence of α-Fe and ϵ-Fe to a value limited by the yield stress ($\sim$1.5 GPa, inferred from the value of c/a lattice parameters ratio in ϵ-Fe; see Sec. IV). This can be in part due to the lattice parameters mismatch between α-Fe and ϵ-Fe, but also to an interaction stress between α and ϵ grains, which relaxes after the completion of the transformation, e.g., in the pure ϵ-Fe or α-Fe phases. The remaining stress can be evaluated using the 2-θ FWHM plotted in Fig. 3. In the reversed α-Fe, the FWHM is $\simeq$0.07°, to be compared to $\simeq$0.05° in the initial α-Fe single crystal. This broadening has two possible sources: broadening of the XRD peak due to the finite size of the diffracting crystals [36], or elastic microstress [27]. Taking into account the observed size of the crystals observed with TEM (Fig. 10), we estimate that the first effect should result in an increase of the FWHM by roughly 0.003°. The remaining broadening corresponds to an elastic microstress of $\sim$0.3 GPa (see Ref. [27] for the method of evaluation of microstress, and Ref. [37] for the elastic parameters in α-Fe). This stress can be due to the dislocations stress field in the sample.

On pressure decrease, most of the grains of ϵ-Fe transformed back to the initial variant of α-Fe. This is unexpected in the case of an ϵ-α transformation, where the six initial variants in ϵ-Fe should produce 13 variants in the reverse α-Fe (Fig. 6). This could be driven by a $\alpha - \alpha$ variant interface energy promoting the reversion into the initial α variant. However, it is not clear why this effect should affect the reverse transition only. The reversion to the original variant could also have been driven by elastic energy associated with defects, for instance dislocations which were common to the α and ϵ phases. Returning to the initial α phase also relaxes internal stresses at the α-ϵ interface. The absence of them, e.g., at the sample surface, could ease to the formation of new variants.

To conclude, we have characterized the α-Fe $\leftrightarrow$ ϵ-Fe transformation under pure hydrostatic compression. Its large hysteresis confirms its martensitic character and the transition range is (14.9 GPa; 17 GPa) for the forward transformation, and (12.0 GPa; 9.2 GPa) for the reversion. The direct transformation follows the Burgers path with no variant selection. Large plastic deformation appears during the first transformation, as indicated by the broadening of XRD rocking curves, together with an elastic stress limited by the yield stress of iron. TEM *ex situ* analysis suggests that the ϵ-Fe microstructure consists of lenticular-shaped grains. On the reverse transition, a drastic variant selection is observed: the crystal almost completely returns to the initial variant, yielding a reversible behavior which is usually observed in shape-memory alloys. This selection is likely to be due to defects and strains created by the direct transformation.

ACKNOWLEDGMENTS

The authors acknowledge the ESRF for provision of beam time under Proposal No. HS-4605. We thank C. Pépin for the help in the synchrotron experiment and P. Loubeyre and B. Amadon for discussions. The authors wish to thank D. Troadec, IEMN, CNRS, Université Lille 1, for the focused ion beam sample preparation and M. Addad, UMET, CNRS, Université Lille 1, for assistance with scanning electron microscope images.

[1] D. Bancroft, E. L. Peterson, and S. Minshall, J. Appl. Phys. **27**, 291 (1956).
[2] P. M. Giles, M. H. Longenbach, and A. R. Marder, J. Appl. Phys. **42**, 4290 (1971).
[3] L. M. Barker and R. E. Hollenbach, J. Appl. Phys. **45**, 4872 (1974).
[4] K. Bhattacharya, S. Conti, G. Zanzotto, and J. Zimmer, Nature (London) **428**, 55 (2004).
[5] A. Lew, K. Caspersen, E. A. Carter, and M. Ortiz, J. Mech. Phys. Solids **54**, 1276 (2006).
[6] W. A. Bassett and E. Huang, Science **238**, 780 (1987).
[7] S. Merkel, H. R. Wenk, P. Gillet, H.-K. Mao, and R. J. Hemley, Phys. Earth Planet. Inter. **145**, 239 (2004).
[8] L. Miyagi, M. Kunz, J. Knight, J. Nasiatka, V. Voltoni, and H.-R. Wenk, J. Appl. Phys. **104**, 103510 (2008).
[9] C. S. Yadav, G. Seyfarth, P. Pedrazzini, H. Wilhelm, R. Cerny, and D. Jaccard, Phys. Rev. B **88**, 054110 (2013).
[10] D. H. Kalantar, J. F. Belak, G. W. Collins, J. D. Colvin, H. M. Davies, J. H. Eggert, T. C. Germann, J. Hawreliak, B. L. Holian, K. Kadau, P. S. Lomdahl, H. E. Lorenzana, M. A. Meyers, K. Rosolankova, M. S. Schneider, J. Sheppard, J. S. Stölken, and J. S. Wark, Phys. Rev. Lett. **95**, 075502 (2005).
[11] L. Dougherty, I. G.T. Gray, E. Cerreta, R. McCabe, R. Field, and J. Bingert, Scr. Mater. **60**, 772 (2009).
[12] S. J. Wang, M. L. Sui, Y. T. Chan, Q. H. Lu, E. Ma, X. Y. Pei, Q. Z. Li, and H. B. Lu, Sci. Rep. **3**, 1086 (2013).
[13] W. G. Burgers, Physica **1**, 561 (1934).
[14] K. J. Caspersen, A. Lew, M. Ortiz, and E. A. Carter, Phys. Rev. Lett. **93**, 115501 (2004).
[15] A. Dewaele, P. Loubeyre, F. Occelli, M. Mezouar, P. I. Dorogokupets, and M. Torrent, Phys. Rev. Lett. **97**, 215504 (2006).
[16] J. B. Liu and D. D. Johnson, Phys. Rev. B **79**, 134113 (2009).
[17] O. Mathon, F. Baudelet, J.-P. Itié, A. Polian, M. d'Astuto, J.-C. Chervin, and S. Pascarelli, Phys. Rev. Lett. **93**, 255503 (2004).
[18] B. Dupé, B. Amadon, Y.-P. Pellegrini, and C. Denoual, Phys. Rev. B **87**, 024103 (2013).
[19] S. Mankovsky, S. Polesya, H. Ebert, W. Bensch, O. Mathon, S. Pascarelli, and J. Minár, Phys. Rev. B **88**, 184108 (2013).
[20] R. Boehler, N. V. Bargen, and A. Chopelas, J. Geophys. Res. **95**, 21731 (1990).
[21] D. L. Farber, D. Antonangeli, C. M. Aracne, and J. Benterou, High Press. Res. **26**, 1 (2006).
[22] H.-K. Mao, J. Xu, and P. Bell, J. Geophys. Res. **91**, 4673 (1986).
[23] F. Datchi, R. LeToullec, and P. Loubeyre, J. Appl. Phys. **81**, 3333 (1997).

[24] A. Dewaele, M. Torrent, P. Loubeyre, and M. Mezouar, Phys. Rev. B **78**, 104102 (2008).
[25] A. Dewaele, J. H. Eggert, P. Loubeyre, and R. LeToullec, Phys. Rev. B **67**, 094112 (2003).
[26] F. Datchi, P. Loubeyre, and R. LeToullec, Phys. Rev. B **61**, 6535 (2000).
[27] A. Dewaele and P. Loubeyre, High Press. Res. **27**, 419 (2007).
[28] S. Klotz, J. Chervin, P. Munsch, and G. LeMarchand, J. Phys. D: Appl. Phys. **42**, 075413 (2009).
[29] F. M. Wang and R. Ingalls, Phys. Rev. B **57**, 5647 (1998).
[30] H.-K. Mao, J. Shu, G. Shen, R. Hemley, B. Li, and A. Singh, Nature (London) **396**, 741 (1998).
[31] S. Merkel, M. Gruson, Y. Wang, N. Nishiyama, and C. Tome, Modelling Simul. Mater. Sci. Eng. **20**, 024005 (2012).
[32] J. Hawreliak, J. D. Colvin, J. H. Eggert, D. H. Kalantar, H. E. Lorenzana, J. S. Stolken, H. M. Davies, T. C. Germann, B. L. Holian, K. Kadau, P. S. Lomdahl, A. Higginbotham, K. Rosolankova, J. Sheppard, and J. S. Wark, Phys. Rev. B **74**, 184107 (2006).
[33] C. Jourdan, J. Gastaldi, P. Marzo, and G. Grange, J. Mater. Sci. **26**, 4355 (1991).
[34] O. Castelnau, M. Drakopoulos, C. Schroer, I. Snigireva, A. Snigirev, and T. Ungar, Nucl. Instrum. Methods A **467–468**, 1245 (2001).
[35] D. Viladot, M. Veron, M. Gemmi, F. Peiros, J. Portillo, S. Estrades, J. Mendoza, N. Llorca-Isern, and S. Nicolopoulos, J. Microscopy **252**, 23 (2013).
[36] A. Guinier, *X-ray Diffraction in Crystals, Imperfect Crystals, and Amorphous Bodies* (Dover, New York, 1994).
[37] G. Simmons and H. Wang, *Single Crystal Elastic Constants and Calculated Aggregate Properties: A Handbook* (MIT Press, Cambridge, MA, 1971).